Space Science Reviews (2024) 220:86
https://doi.org/10.1007/s11214-024-01120-y

SPECIAL COMMUNICATION

The Juno ASC as an Energetic Particle Counter

Troelz Denver[1] · Julia Sushkova[1] · John L. Jørgensen[1] · Leonardo Ghizoni[1] · Matija Herceg[1] · Christina Toldbo[1] · Mathias Benn[1] · Peter S. Jørgensen[1] · René Fléron[1] · J.E.P. Connerney[2,3] · Heidi N. Becker[4] · Scott J. Bolton[5]

Received: 19 February 2024 / Accepted: 25 October 2024

Abstract

The Juno spacecraft completed 35 successful orbits around Jupiter from orbit insertion in 2016 through the end of its prime mission phase in 2021. The Advanced Stellar Compass (ASC) and associated Camera Head Units (CHUs) comprise a dedicated attitude sensing system of the Magnetic Field Investigation (MAG), one of Juno's scientific payloads. The CHU is a CCD-based camera and is inherently susceptible to ionizing radiation. An energetic charged particle penetrating the camera head electronics shielding will deposit its energy and liberate charges in the charge wells. These events will register as isolated bright pixels in the integrated star tracker source images, and are distinguishable from optical sources that illuminate a number of collocated pixels spanning the imager's point spread function. By simply counting the number of such isolated bright pixels, an estimate of the number of charged particles penetrating the CCD can be established, eventually constraining the local external omnidirectional radiation flux (omniflux). The ASC performs the bright pixel count onboard and includes this count rate with the attitude telemetry, providing an energetic particle omniflux measurement at high time resolution. We describe here this additional functional capability of the ASC, including the filtering required to isolate the unbiased attitude cycles, the calibration required to circumvent count statistics effects, and the calibration of the sensor sensitivity, as well as the attenuation efficacy of the sensor shielding mass. Finally, we discuss the potential of the omniflux product for radiation field mapping as well as a proxy for investigating physical phenomena otherwise unattainable.

Note by the Editor: This is a Special Communication. In addition to invited review papers and topical collections, Space Science Reviews publishes unsolicited Special Communications. These are papers linked to an earlier topical volume/collection, report-type papers, or timely papers dealing with a strong space-science-technology combination (such papers summarize the science and technology of an instrument or mission in one paper).

✉ T. Denver
td@space.dtu.dk

1 Technical University of Denmark, DTU Space, Kgs. Lyngby, Denmark

2 Space Research Corporation, Annapolis, MD, USA

3 NASA Goddard Space Flight Center, Greenbelt, MD, USA

4 Jet Propulsion Laboratory, California Intsitute of Technology, Pasadena, CA, USA

5 Southwest Research Institute, San Antonio, TX, USA

Published online: 06 November 2024

Keywords Jupiter · JUNO · ASC · Radiation monitoring · Jovian radiation field

1 Principles of the Measurements

The Juno spacecraft (Bolton et al. 2018) was inserted into a highly elliptical, near polar orbit about Jupiter on July 4th, 2016. During its primary mission, 35 successful orbits around Jupiter were recorded (orbital duration of 53.4 days and perijove altitude of roughly 0.1 Rj). The orbit period was chosen with regard to the rotation period of Jupiter, to eventually envelope Jupiter in a grid-like set of observations near periapsis separated in longitude by roughly 11°. Since the magnetic field trapping the main radiation belt of trapped electrons is tilted roughly 10° from the spin axis, this trajectory ensures that a broad swath of Jupiter's high radiation region is scanned during each orbit.

Juno avoided the most severe radiation regions during the prime mission phase by taking advantage of the gap between the radiation belt region and the planet itself. As the line of apsides evolves due to the oblateness of Jupiter, the Juno trajectory passes through electron radiation belt regions with increasingly higher fluxes of ultra-relativistic electrons during the mission. The Juno magnetic field experiment (Connerney et al. 2017) sensors are positioned on the magnetometer boom at the end of one of Juno's three solar arrays, 8 and 10 meters from electromagnetic disturbances from the spacecraft body (see Fig. 1). The sensor packages consist of two identical magneto-optical benches (MOB), each with one *Flux Gate Magnetometer* (FGM) and two *Advanced Stellar Compass* (ASC) star tracker optical *Camera Head Units* (CHU). Each CHU is equipped with optics and a charge coupled device (CCD) image sensor with support electronics in a protective enclosure (Fig. 1). The dedicated radiation shielding of the CCD and support electronics, along with the standard CHU enclosure and proximate spacecraft mass, containing a combination of Al, Ti, Cu, Au, W, quartz, ceramics, and other materials, efficiently protects the sensitive electronics from different kinds of radiation encountered in the space environment. The shielding mass substantially reduces the number of electrons and protons reaching the sensitive semiconductor components. However, in harsh radiation regions, penetrating radiation will reach the CCD sensor die and liberate secondary electrons along the ionizing track. If this happens within the sensitive volume, the radiation-induced electrons will be trapped, held, and read, in the same way as the photoelectrons. The CCD registers these charges as bright pixels that appear sporadically in individual images, disappearing in the next ones. CCD imagers may also develop pixels that are persistently bright, failed pixel elements that are routinely identified and excluded.

As a radiation particle counter, the ASC registers interactions between the CCD Si die and the ionizing particle (typically electron or proton), though it can't discern whether the particle is positively or negatively charged. The count rate is recorded per image frame during the entire mission. The data thus acquired have a high time resolution (4 Hz), but contain only ionizing particle impact events, with no direct information in regard to the particle species or its energy.

The other types of ionizing radiation (neutrons, X-rays) are not considered in this article though in principle a CCD would detect them. Hard X-Rays, being highly penetrating, are less ionizing, so their input into counts would not be detectable. Soft X-Rays, primary or secondary (e.g. from the spacecraft main body), being highly ionizing, would not penetrate through the shielding to the CCD die (Hubbell and Seltzer 2004). As Juno is solar-powered and does not have any decay source, neutron flux is infinitesimal compared to the Jovian trapped radiation.

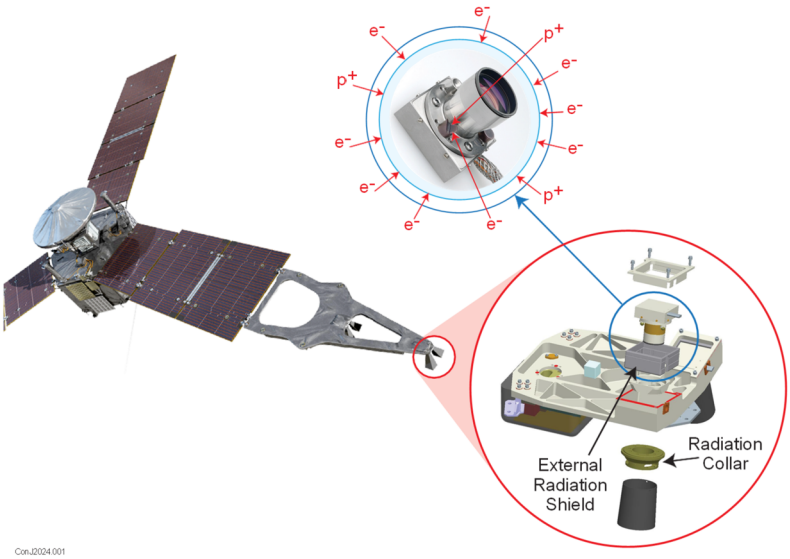

Fig. 1 Left: Mounting position of the ASC camera head units on the Juno boom-tip. Lower right: The magneto-optical bench including mass radiation shielding collars. Upper center: Conceptual view of the CHU inside the mass shielding, where penetrating radiation reaches the CCD

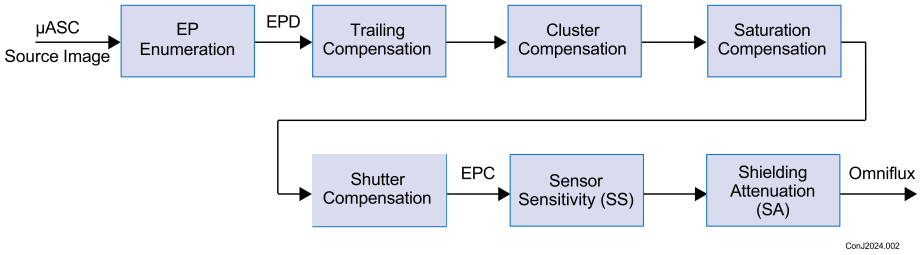

Fig. 2 Processing flow for deriving the external omniflux from the μASC star tracker source images

The objective of this paper is to describe the processing and calibration that allow quantification of the external omnidirectional flux of ionizing radiation particles (= *omniflux*) from the e*nergetic particle detections* (EPD) observed in the star tracker images. The process, as observed from the CCD sensor images and out, can be broken down as shown in Fig. 2.

The *Energetic Particle* (*EP*) *Enumeration* counts the number of image objects with an area less than or equal to 4 pixels. By design, focal objects (stars) will spread photons over a multiple-pixel point spread function, and typically also exhibit a larger extent due to smearing of the image as the spacecraft spins (2 rotations per minute) during the image integration period (0.25 sec). This processing is performed within the star tracker flight software (FSW) and is telemetered to ground yielding the EPD. The *Trailing Compensation* accounts for the EP trails that are larger than 4 pixels. These are typically observed within the heavier radiation environments. The *Cluster Compensation* process compensates for heavy radiation regimes where EPs interacting with neighbor pixels in the pixel grid are counted as a single hit. The star tracker will stop the EP enumeration when the number of stellar candidate

objects (area >= 5 pixels) has reached a preset maximum of 200. This occurs in heavy radiation environments from both trailing and clustering effects. The S*aturation Compensation* is performed to estimate the true EPD in such a saturation event. The electronic *Shutter Compensation* is used in the star tracker operation to reduce the effective integration time on the CCD. This is used to suppress saturation in severe radiation environments and expand the dynamic range of the radiation count. Since the CCD integration layer is only sensitive to EP during the effective integration period, the count needs *Electronic Shutter Compensation* accordingly.

Following these four compensation activities, the number of EPs that have deposited ionization traces on the CCD above detection threshold (8 DN ∼= 100 electrons) per time unit has been established. This number is referred to as *Energetic Particle Countrate* (EPC).

The Energetic Particle Countrate (EPC) is directly proportional to the integral omnidirectional flux (F) of the primary cosmic radiation (electrons, or protons, or both) within the detection energy range compensated for the S*hield Attenuation* (SA) and S*ensor Sensitivity* (SS) factors.

$$EPC = \frac{F_{e^-,E>E_{min}}}{SA_{e^-} \cdot SS_{e^-}} + \frac{F_{p^+,E>E_{min}}}{SA_{p^+} \cdot SS_{p^+}} \tag{1}$$

Here $F_{e-,E>E_{min}}$ and $F_{p+,E>E_{min}}$ [particles/cm^2/s] are the external omnidirectional flux of electrons and protons above the detection threshold E_{min} for electrons and protons respectively. The energy thresholds are discussed in more detail in Sect. 3.1. The Shielding Attenuation (SA) factor is a unitless quantity representing the mean fraction between the external omnidirectional integral flux and the resulting penetrating integral fluxes that break through the ASC CHU shielding. The SA is described in details in Sect. 3.1. Note that in this context SA is >1, such that the quantity defines a multiplyer used to compensate for the saturation through the shielding.

For proton-dominated radiation environments (e.g. the Earth's trapped radiation), the first term is normally neglected, as SA_{e-} is high even for the minimal CHU shielding in the standard CHU configuration. Conversely, for most regions of the Juno environment, where fluxes of relativistic electrons are a few orders of magnitude higher than those of protons at the corresponding threshold energies ($F_{e-,E>E_{min}} \gg F_{p+,E>E_{min}}$, Divine and Garrett 1983, Jun and Garrett 2005), the last term in the equation can be dismissed.

Thus, the omnidirectional flux of ultra-relativistic electrons along the Juno trajectory (or more commonly, high energy electrons and protons in any orbit) above a certain sensitivity threshold ($E > E_{min}$) may be deduced from the star tracker source images using the described procedure.

2 Sensor Hardware

The imaging sensor used for the energetic particle detection is a front illuminated, interline transfer CCD. During normal operation, incoming photons in the 300-740 nm wavelength range liberate electrons in the sensor die. These electrons are maintained in the charge wells (one well for each pixel) of the integration layer. A sketch of the CCD principle is shown in Fig. 3.

After a suitable integration period (typically 125 ms), the accumulated charges are all flushed in parallel to a read-out "layer" and the next image (and EPD) integration starts. During the following integration period, the read out layer is read out row-wise via first a

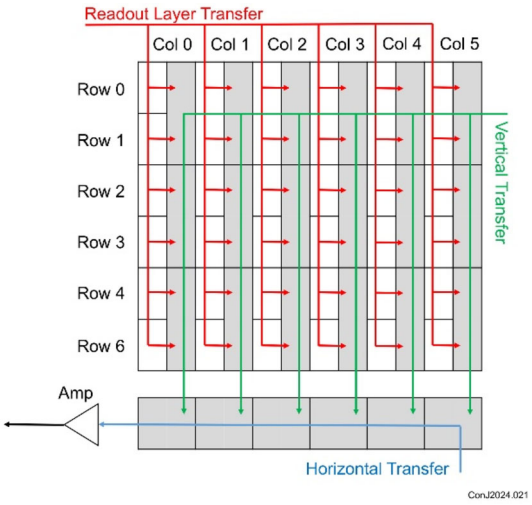

Fig. 3 Principle of CCD operation. The photosensitive integration-layer areas (pixels) are shown in white, the covered readout-layer areas are grayed. The sketch shows integration of the first (even) image field

vertical and then a horizontal readout. A full image is generated typically at 4 Hz, which also determines the temporal resolution of the particle count data. Further, the image sensor is operated interlaced using field integration, such that:

- Even image rows (0, 2, 4, . . .) are integrated for the first half of the effective integration period by merging pixels in row 0 and 1, 2 and 3, 4 and 5, etc.
- Odd image rows (1, 3, 5, . . .) are integrated for the second half of the effective integration period by merging pixels in row 1 and 2, 3 and 4, 5 and 6, etc.

The sensor also supports an electronics shutter. When asserted, all accumulated charges from the integration layer are flushed to the drain channels allowing for an accurate control of integration periods down to microseconds.

A typical Jupiter passage is shown in Fig. 4. The speckle type noise from penetrating high energy electrons is clearly visible in the star tracker image (top right) and by counting the number of speckle pixels in each image, compensating for electronic shutter usage and applying the calibration, and estimate of the external electron environment is readily obtained.

Several parts of the sensor image chain are sensitive to ionizing radiation. The penetrating radiation may interact in the CCD integration layer, in the CCD readout layer, and in the operational amplifier stages. To enable an accurate absolute determination of the environmental radiation conditions, the sensitivity of the various stages must be characterized.

This work focuses specifically on utilizing the heavily shielded ASC star tracker hardware on-board the Juno spacecraft for radiation monitoring purposes. Any high sensitivity camera, CCD or Active Pixel Sensor (APS) based, may in principle be used for the purpose. Anyone intending to use the ASC radiation count rate observations is encouraged to familiarize themselves with the following sections. Similarly, any reader contemplating the design or use of a radiation monitoring system with an image sensor as the sensing element may find in the following sections information relevant for the chosen hardware and application.

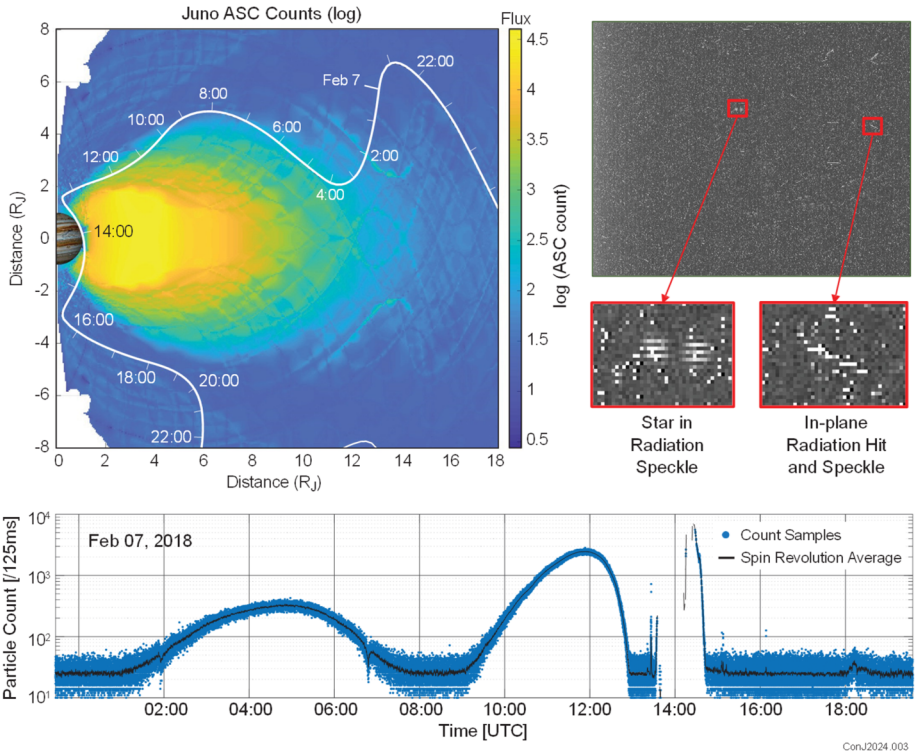

Fig. 4 Top left: The PJ-11 trajectory of Juno overlaid on a Jovian system magnetic equatorial projection frame. Top right: CHU Image acquired in a heavy radiation region showing both stars and radiation-induced speckle and in-plane tracks. Bottom: The PJ-11 time series along a trajectory showing the energetic particle count rate as a function of time along Juno's trajectory through the inner magnetosphere. The dark points are an average over 30 s (one spacecraft spin period

3 Calibration

The calibration scheme covers the entire path from count rates on the CCD to the external relativistic electron environment. The goal is to establish the omnidirectional electron flux environment, within the sensitivity range, from the count rates. Progressing from external omniflux to image, the following calibration scheme has been exercised:

- Radiation shield transport model (Shielding Attenuation, SA factor)
- Particle flux to count conversion (Sensor Sensitivity, SS factor)
- Electronic shutter compensation (converts count to count rate)
- Saturation compensation (premature stop of counting)
- Cluster compensation (non-linearity for high count rates)
- Trailing compensation (incorrect classification of EPD as stellar candidates)

3.1 Radiation Shield Transport Model – Shielding Attenuation (SA) Factor

The Shielding Attenuation (SA) factor is the ratio between the external omnidirectional integral electron flux and the penetrating fluxes of electrons and positrons that break through the

shielding. It combines analysis of the instrument's shielding efficacy (geometry and materials) and knowledge of the nature and hardness of the external radiation source. Therefore, the first step in acquiring the SA is to compute the penetrating particle fluxes that reach the ASC CCD.

The Juno ASC design encompasses a mass- and volume- efficient approach to radiation shielding, meeting operational and performance requirements of the Juno mission and prolonging its lifetime in a challenging radiation environment. The ASC design employs several materials to meet radiation shielding and functional requirements, e.g., gold (especially efficient shielding efficacy against relativistic electrons), titanium, quartz, aluminum, amongst others. This approach limits the applicability of widely-used modelling techniques such as Ray Tracing, as divergences would be noticeable for electrons with energies >20 MeV. Although computationally efficient, the Ray Tracing technique is an approximation as it ignores angular scattering of particles (particularly important for electrons), and the true angular distribution of secondary radiation is not explicitly treated. In addition, the technique involves treating all materials as being the equivalent of one material type and therefore is not suitable for quantifying graded shielding or dose-enhancement effects (ECSS 2010). Therefore, we employed the more detailed Monte Carlo radiation modelling approach, which considers the actual particle interactions that occur within the specific materials that make up the CHU and its immediate surroundings, as detailed in an accurate solid model of the CHU and its environment.

A set of Geant4 simulations with the Forward Monte Carlo method was performed to determine the shielding efficacy of the ASC CHU against high-energy electrons. In each of the simulations we directed a source of monoenergetic electrons onto the solid model geometry and computed the number of electrons and positrons that hit the ASC CCD. The simulated external source is characterized by:

- A spherical monoenergetic electron source (primaries) with omnidirectional fluxes by means of a cosine-law;
- An energy range of 3 MeV to 1 GeV, with 1 simulation performed for each energy increment. The energies simulated are [3, 5, 10, 15, 20, 25, 30, 40, 50, 60, 80, 100, 150, 200, 400, 600, 800, 1000] MeV;
- A total of 1E+09 primaries per simulation to ensure high-quality statistics.

A high-fidelity mass model of the entire instrument suite illustrated in Fig. 5 was used, including the ASC CHUs with baffles, optical bench, and flux gate magnetometer. All the materials and respective cross-sections are based on the National Institute of Standards and Technology (NIST) comprehensive database information (Berger et al. 2017) and implemented via the G4NistManager class from Geant4. The particle interactions and processes use the default Physics List provided by Geant4, *FTFP_BERT* (Allison et al. 2016), with the addition of the most precise Electromagnetic Physics package, *EM Opt4* (*_EMZ* extension). The final Physics List implemented is *FTFP_BERT_EMZ* (Ivanchenko et al. 2019). The target of the simulations was defined as the active region of the ASC CCD (752 × 580 pixels), with an overall area of 31.13 mm^2.

The simulation output consists of the number of electrons (both primary and secondary) and positrons impacting the target. The simulations were configured for counting only incident electrons and positrons that reach the surface of the CCD, disregarding any secondaries that are eventually produced inside the CCD volume, as these are already considered in the Sensor Sensitivity (SS) factor presented in Sect. 3.2.

Figure 6 presents the normalized shielding efficiencies as function of the initial energy of the external primary electrons for the ASC CHU, consisting of the ratio of particle fluxes

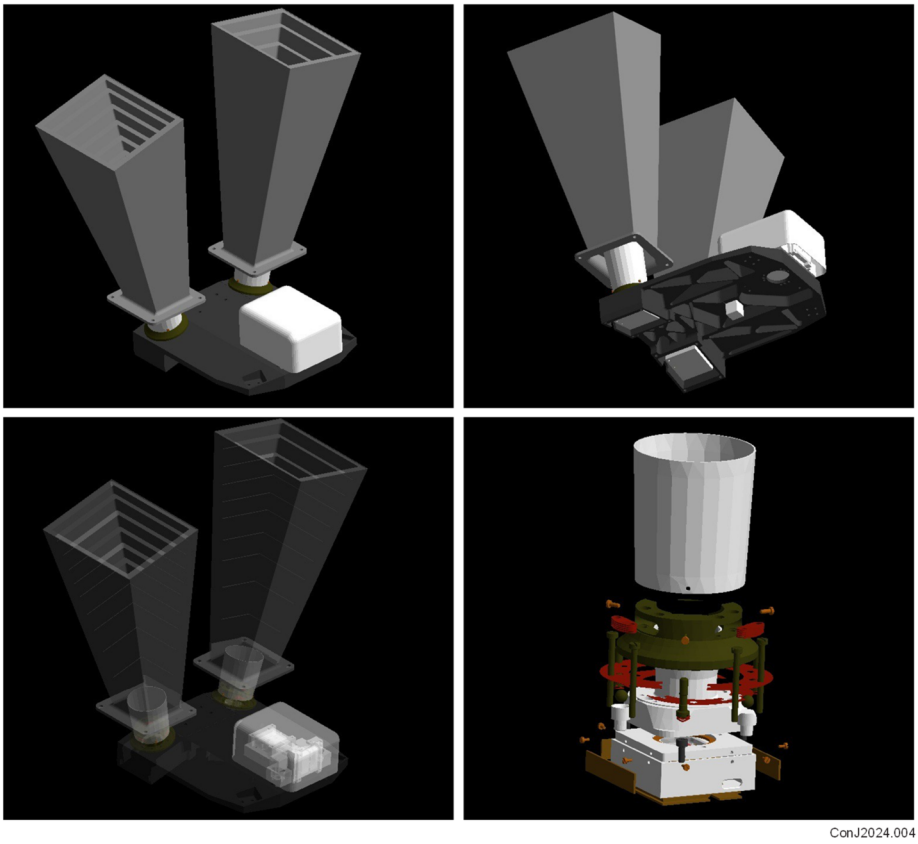

Fig. 5 Geant4 mass model of the ASC star tracker and fluxgate magnetometer instrument suites

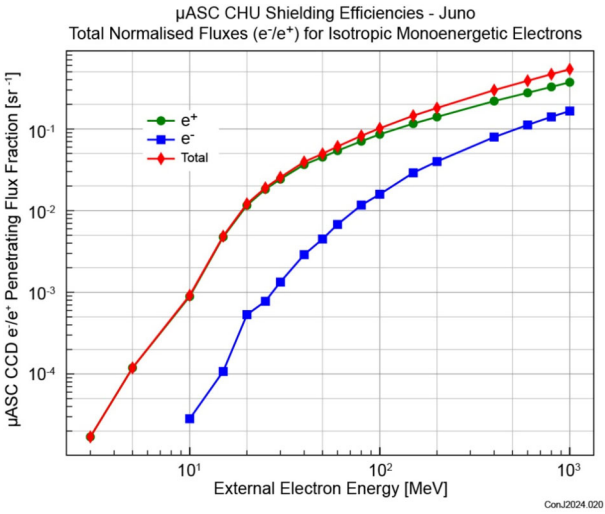

Fig. 6 Efficiencies for the ASC CHU, with energies ranging from 3 MeV to 1 GeV. The efficiencies include contributions of both electrons and positrons. Each point consists of an independent simulation with monoenergetic and omnidirectional electron sources

reaching the CCD and the external primary fluxes. The individual contributions from electrons and positrons to the total penetrating fluxes is shown in detail. Each point in the graph represents an independent simulation. The positron contributions become appreciable for $>$ 20 MeV, energy beyond which pair production clearly becomes the dominant process, reaching $\sim$36% of the total counts at 1 GeV.

It is worth noting that the results presented herein are largely comparable to those of Becker et al. (2017), with relatively minor disagreements between them originating from small differences in the solid models employed in the analyses.

The Shielding Attenuation (SA) factor is finally computed by taking the fraction between the energy integral of the external differential electron fluence predictions, and the corresponding ASC CHU penetrating fluences. The latter are computed by multiplying the external differential electron fluences with the shielding efficiency curve presented in Fig. 6, and integrating over energy within a given range of interest.

The following relation is used for computing the Shielding Attenuation (SA) factor:

$$SA_{e^-} = \frac{\int_{E_{th}}^{1\ \mathrm{GeV}} \Phi_{External_{e^-}}\, dE}{\int_{E_{th}}^{1\ \mathrm{GeV}} \Phi_{Penetrating_{e^\pm}}\, dE} \tag{2}$$

where $\Phi_{External}$ and $\Phi_{Penetrating}$ are the external and penetrating differential electron fluxes respectively, E_{th} the energy threshold, and dE the energy step.

The shielding will effectively block external electrons $<$10 MeV as shown in Fig. 6. Any particle penetrating to the CCD with sufficient energy will generate an EPD. To derive an effective threshold for energy sensitivity, the shape of the external flux spectrum is needed. The D&G83 (Divine and Garrett 1983) and GIRE (Galileo Interim Radiation Environment, Garrett et al. 2003) models were used as the reference external electron trapped radiation sources. The GIRE model was used for energies up to 30 MeV, while the D&G83 model was applied for the]30 MeV, 1 GeV] range. The following environment was used as input to Spenvis using the above models to derive the electron fluence:

- The Juno flight trajectories for orbit 1-35
- Limited to $+/-$5.5 h from closest approach to Jupiter
- 1 data point per 30 s (only the spectrum shape is relevant)

Figures 7 and 8 present the differential and integral forms, respectively, for the external and penetrating fluences. It is important to note that:

- The penetrating fluence curves (in red) represent the total counts of electrons or positrons produced from the respective external electron energy. It does not represent the energy of the penetrating particles.
- At higher energies the penetrating fluences become higher than the respective external ones. The higher the incoming electron energy, the more it will produce secondaries throughout the camera shielding. Such secondaries also reach the CCD and are added to the total count, as long as the energy is equal or higher than the Silicon ionization energy, $\sim$8 eV.
- The vertical axis represents the reduced trajectory dataset including both 30 s decimation and reduction to $+/-$5.5 h from closest approach. The magnitude is therefore not representative for the total mission fluence.

From Fig. 8 it is observed that the integral penetrating fluence is flat up to 20 MeV, indicating that electrons with primary energy about 20 MeV give the major input to the EPDs in the images.

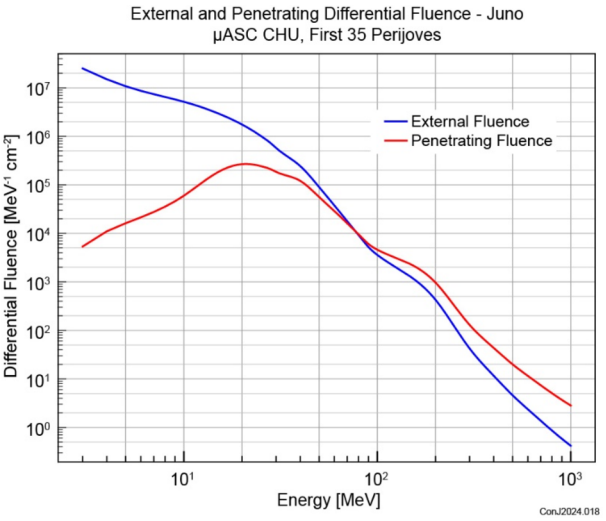

Fig. 7 External and penetrating differential fluences for the ASC CHU as exposed to accummulated over orbit 1 through 35

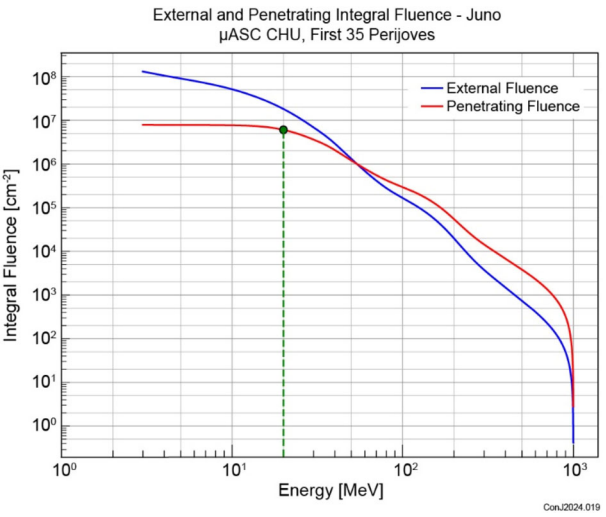

Fig. 8 External and penetrating integral fluences for the ASC CHU as exposed to accummulated over orbit 1 through 35

The SA factor is computed using equation (2) with an energy threshold $E_{th} = 20$ MeV for the fluence model leading to a shielding attenuation $SA_{e-} = 3.00$.

3.2 Particle to Count Conversion – Sensor Sensitivity (SS) Factor

For the task of using the ASC with its CCD detector as a particle (electron) counter, we could limit the problem to ionizing defects in Si within the "detection volume". Each electron from the environment that passes through the shielding and travels inside the silicon CCD die, gradually loses its kinetic energy (∼0.3-3 keV/μm for a wide range of the incident electrons energies) via soft and hard collisions, creating ionizing defects (electron-hole pairs) along its track in the semiconductor. The stopping of fast electrons in substance leads not only to ionization losses of energy but also to scattering. Electrons frequently are deflected at large angles due to their small relative mass, and the smaller the energy of an incident electron,

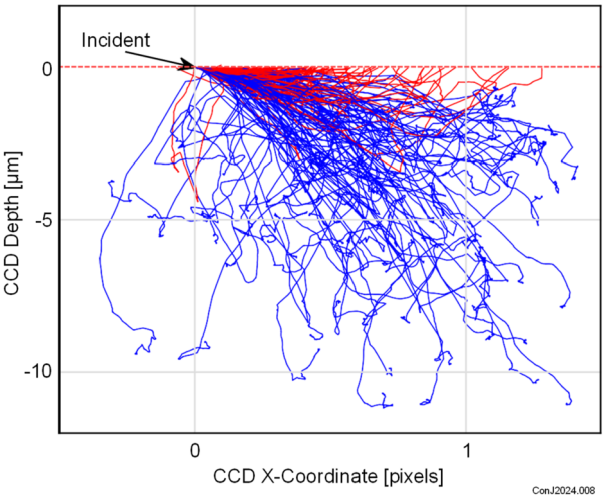

Fig. 9 Side (XZ) view of electron tracks produced in a silicon CCD die, inclined (80°) incident, 220 electrons with 0.04 MeV primary energy are tracked. Backscattered electrons are shown in red. The vertical lines indicate pixel boundaries, while the horizontal dashed lines indicate depth

the larger is its mean angular deflection from the initial direction. Due to multiple scattering, the trajectory of electrons has a complex shape, and its total traversed length ranges from ∼1.5 to ∼4 times the thickness of the layer in question, had it not deviated from its initial direction (Vavilov and Ukhin 1977). The liberated electrons can then migrate both in and out of the "detection volume", as well as recombine. The "detection volume" in the XY plane is approximately the pixel physical area (8.6×8.3 µm^2) times its depth of ∼10 µm (which in principle varies with temperature). Most of the generated electrons have low energy and will be trapped within 1 µm; electrons generated further from the detection volume have a higher probability of recombining and thus not being collected. Therefore, the detection volume can be equated to that of a single pixel.

If the read radiation noise signal in one and only one CCD pixel during one imaging cycle is sufficiently higher than the dark noise, this will be counted as an EPD event. However, if one incident particle creates this sufficiently high radiation noise signal in more than one CCD pixel, they could be detected (but not counted) as separate EPD events.

The amount of the incident electrons required to produce one counted "event" would thus depend on a number of factors: The probability of the ionizations to occur inside or in the vicinity of the pixel/active region, the number and placement of pixels with radiation-liberated electrons, the dark noise level, the number and placement of pixels illuminated, as well as the method of counting the events, including the algorithm suppressing the multiple-pixels events.

In order to calibrate the system and compute the Sensor Sensitivity factor SS, both computer simulations and irradiation testing were performed.

Computer simulations utilizing Monte Carlo tracking of electrons inside a CCD die were performed with the Casino tool (Drouin et al. 2007). Trajectories of electrons with primary energy in the range of 0.01 to 10 MeV were simulated for a monoenergetic electron beam at varied angles of incidence. The simulation example given in Fig. 9 illustrates the situation when significant radiation noise is deposited in multiple pixels.

We also performed experimental testing of the radiation noise signatures for the Juno ASC under different environmental and driving conditions using a calibrated Sr-90 (double beta minus) radioactive source. The source provides a stable beam of electrons with energy spectrum with means 1 MeV and up to 2.2 MeV, making it a suitable source for such tests.

Radiation noise images were acquired in our experimental setup with different electron fluxes, CCD temperatures, incident angels, artificial star stimulations, integration time constants, electronic shutter settings, etc. The cover glass from the CCD under test was removed, so that tilting the detector would not change the energy spectrum of the primary beam. The acquired images were analyzed for the radiation induced noise (generating count rates) in the same fashion as the Juno flight instrument processes source images.

The testing and analysis we performed characterized the CCD response to the known high energy electron irradiation. For the Juno ASC instrument, Juno operation temperature and Juno particle counter software, the following relation is established: $SS_{e^-} = 300 + / - 50$ e$^-$/cm^2/s, or in other words, placing the CCD under an electron beam of $F =$ 3E+05 e$^-$/cm^2/s, one could expect to arrive at $EPC = F/SS = 1000$ in one image.

3.3 Electronic Shutter Compensation

The electronic shutter allows flushing the integration layer (white areas in Fig. 3) thereby reducing the effective shutter exposure. Since both the integration layer, the read-out layer (grayed ares in Fig. 3), and the support electronics are sensitive to ionizing radiation, the relative sensitivity of each of these components to the electronic shutter time must be established. For this purpose, a test setup was realized in the laboratory at the Technical University of Denmark with which it was possible to irradiate the flight-like CHU (including chipset) with electrons. Manipulating the electronic shutter with 5 different settings allowed an overdetermination of the relative sensitivity. It was found that without shutter usage ~70% of the particles were interacting in the shutter dependent integration layer (accummulating EPD over T_{shut}), while ~30% of the particles were interacting in the shutter independent readout layer and support electronics (continuously accummulating EPD effectively over T_{int} for each image cycle). The shutter compensation is established as a constant K_{shut} to multiply onto the count from the following relationship:

$$K_{Shut} = \frac{T_{Int}}{f \cdot T_{Shut} + (1 - f) \cdot T_{Int}} \tag{3}$$

where T_{Int} is the formal integration time used for both integration and readout, when no electronic shutter is employed, T_{Shut} is the actual shutter time, and f is the relative sensitivity of the integration layer (measured to 0.70). Note that when no electronic shutter is used, i.e. $T_{Shut} = T_{Int}$, the shutter compensation constant K_{Shut} equals 1.

3.4 Saturation Compensation

The saturation effect occurs in heavy radiation environments where excessive trailing occurs and ionization trails larger than 4 pixels are identified as focal (stellar candidate) objects. The immediate consequence of the appearance of many large image objects is that the instruments stellar candidate count (SCC) reaches the preset count limit (200) and the limit is reported along with the (premature) radiation count. The calibration factor for such is found using an abundance of source images acquired from the Juno trackers in heavy radiation environments. Re-processing the source images on ground without the 200 object count limit, the unlimited SCC (size $>$ 4 pixels) and EPD counts (size $<=$ 4 pixels) are established. A model of this relationship using a 4th order polynomial fit is given in equation (4).

$$SCC\,(EPDC) = \begin{cases} 4.5 \cdot 10^{-14} EPDC^4 + 3.0 \cdot 10^{-6} EPDC^4 + 10.5, & \text{no shutter} \\ 4.2 \cdot 10^{-14} EPDC^4 + 3.3 \cdot 10^{-6} EPDC^4 + 10.5, & \text{shutter} \end{cases} \tag{4}$$

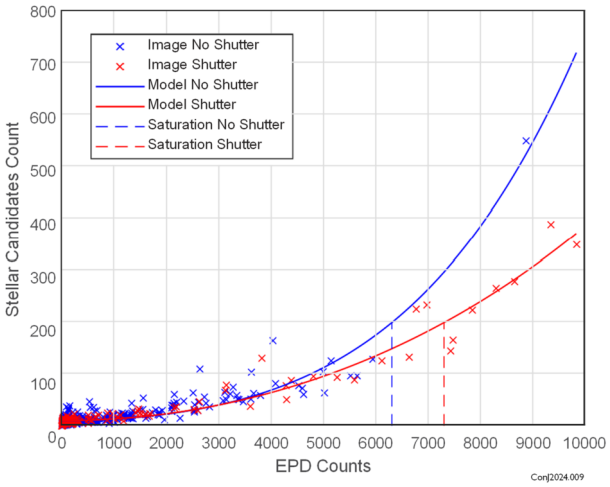

Fig. 10 Generation of saturation compensation model from offline processing of images

Figure 10 summarizes the EPD and stellar candidate count established from the images, the derived model and the saturation levels.

Let F denote the fit model, such that

$$SCC = F(EPDC) \tag{5}$$

where SCC is Stellar Candidates Count and $F(EPDC)$ is the fit function of the Energetic Particle Detection Count ($EPDC$). Assuming a homogenous distribution of both stellar candidates and EPDs in the images, the following relation can be assumed:

$$\frac{EPDC_{Meas}}{EPDC_{True}} = \frac{SCC_{Meas}}{SCC_{True}} \tag{6}$$

In case of saturation the measured Stellar Candidate Count (SCC_{Meas}) equals 200, and using the relation $SCC_{True} = F(EPDC_{True})$, the $EPDC_{True}$ may be found as the largest real root in the equation:

$$F(EPDC_{True}) - \frac{200}{EPDC_{Meas}} EPDC_{True} = 0 \tag{7}$$

Once $EPDC_{True}$ is found, SCC_{True} is derived and used as input for the trailing compensation process. The compensation function is conveniently implemented as a lookup table, employed in the conversion process from energetic particle detections to countrate.

Note that saturation compensation is associated with high error bars. Firstly, the compensation tables are derived from very few data samples (images). Secondly, plotting the non-saturated and saturated data as a time series lead for some orbits to data discontinuities at the transitions. The data points marked as saturated should therefore be used cautiously.

It is further noted that the EPD to SCC relation depends on the star field density in the images. In rich star density regions, i.e. when the star trackers are pointed towards the galactic plane, more true SCCs are present and saturation will occur at a lower radiation flux. The image material used in this section is acquired over the entire primary mission and thus represents the average star density observed, i.e. representatively weighing rich and meagre star fields.

3.5 Cluster Compensation

The clustering effect occurs when two (or more) interactions occur in neighbor pixels. The calibration can be found either analytically using statistics or numerically using Monte Carlo simulations. In this work the latter was selected. For this purpose, an engineering model of the instrument operating the flight software algorithms was used. The instrument was set to operate on a source image captured from Juno during calm radiation conditions. By injecting bright pixels at arbitrary positions, the non-linearity at high count rates were easily characterized and a lookup table providing true count rates as function of reported counts was established. This lookup table is employed in the conversion process from energetic particle detections to countrate.

3.6 Trailing Compensation

The trailing effect originates from particles penetrating the CCD die at grazing incidence. When the particle interacts with five or more pixels the image analysis algorithm classifies and counts the interaction as a stellar candidate. The effect is visible in Fig. 10, where the "stellar candidate count" increase with increasing EPD count.

The derived relation models between the stellar candidate count (SCC) and the EPD count (EPDC) may further be used to derive the compensation. The two relation model each has the form:

$$SCC\,(EPDC) = c_1 EPDC^4 + c_2 EPDC^2 + c_3 \tag{8}$$

where the coefficient c_3 is the average contribution of "true" stellar candidates. The remaining term is thus the contribution from trailing EPD. The compensation can thus be found from:

$$F_{TrailComp}\,(EPDC) = c_1 EPDC^4 + c_2 EPDC^2 + EPDC \tag{9}$$

3.7 Comparison Between ASC Flux and Model Flux

Figure 11 shows a comparison between calibrated ASC flux and flux modeled using GIRE2 (de Soria-Santacruz et al. 2016) from around the closest passage during orbit 11.

It is noted that the calibrated data largely follows the model for $E_{e-} > 20$ MeV but express a somewhat higher flux in the high flux regions.

4 Filtering

Since the prime objective of the instrument is star tracking, the sensor is inherently sensitive to photons in the visible range. For the purpose of omniflux assessment, the photon-generated signal is considered an unwanted noise disturbance and the effect must also be addressed. Since the EPC rate is vastly oversampled, an effective and rather simple way of eliminating photon contamination is to simply eliminate estimates that may suffer from such. Hence, count cycles expressing the following characteristics are suppressed from the final data sets:

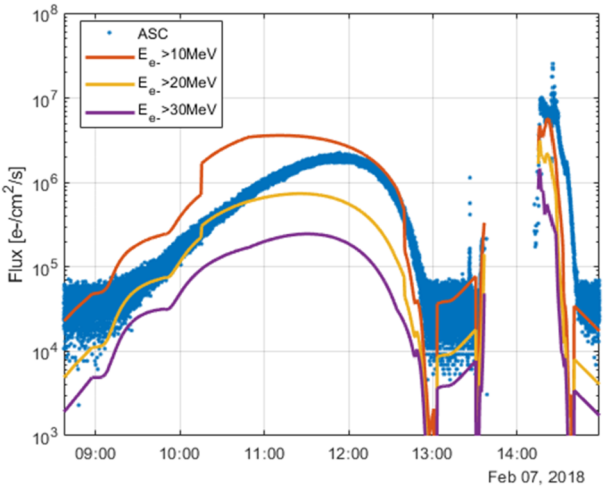

Fig. 11 Comparison between calibrated ASC flux and modeled flux using the GIRE2 model for three different threshold energies

- A Big Bright Object (BBO) is identified in the source image. This signal is intended to indicate when a Jovian moon intrudes upon the CHU field of view, or when the bright Jupiter limb appears close to, or within, the source image. The appearance is signaled in telemetry. The effect is typically that the count rate is underdetermined in BBO images, because a large fraction of the image is photon-contaminated. At high count rates, the effect is less significant. These count measurements are included in the data set, but the BBO identification is signaled, so the user may determine what use to make of it.
- The flight processor keeps track of time spent processing an image in order to prevent spillover into the subsequent image processing interval. When the prescribed processing timeout time is reached, the reported energetic particle count is prematurely rendered in the telemetry. These estimates cannot be meaningfully compensated and are removed from the data.
- A background clamping change is requested by the flight software. The image background (black) is continuously controlled to track temperature dependencies and BBO proximity. A requested change is indicating appearance of a slight photon contamination that may offset the particle count. These estimates are likewise removed from the data.

5 Sensitivity/Dynamic Range

The CHU shielding efficiently absorbs electrons with energy ranges < 5 MeV, and in the Jovian magnetosphere electrons with energies > 20 MeV (in the external environment) will dominate the EPD count (Sect. 3.1). This conclusion follows from consideration of the shielding efficacy of the CHU as a function of energy and the electron spectra in Jupiter's magnetosphere.

Energetic particles may be expected to penetrate in any angle to the plane of the CCD. At high incidence angles, the particle trail may pass through one or more neighbor pixels in the grid leaving a trailing effect. One particle hit may therefore interact with several pixels. Thus, interactions in a neighboring pixel (using the 8 pixels around any pixel) are counted as one incident.

Within rich radiation environments, the counts become numerous enough to interact often with neighboring pixels. Two separate particle hits may even interact with the same

pixel. The sensor software counts pixel neighbor (8-pixel connectivity neighborhood) as one incident. This non-linearity is calibrated, and compensated for, in the post processing.

With sensor images of roughly 436k pixels, around 20k individual interactions may be discerned. In richer radiation environments, too large a number of interactions would appear in neighboring pixels and the ambiguity would be too great for a reasonable particle count. This effect has been circumvented in many of Juno's periapsis passes by applying the electronic shutter, effectively flushing the integration layer after almost the entire integration period, dramatically reducing the EPC.

6 Relativistic Radiation Count Data

Energetic particle data recording was initiated on ASC using the above mentioned techniques prior to Jupiter orbit insertion, and EPC rates have been recorded continuously since then. During the Juno prime mission, spanning the first 35 orbits around Jupiter, the ASC recorded data from all perijove passages, with the exception of PJ-2, during which the spacecraft entered safe mode shortly prior to the passage. The data product from a typical perijove passage (PJ-11) is shown in Fig. 12, and provides an overview of both data potential and the level of details available. See e.g. Connerney et al. (2020) and Herceg et al. (2022) for a detailed analysis of the disturbance signature observed in the leftmost zoom panel where Juno crosses the magnetic field that passes through the Ganymede's orbit.

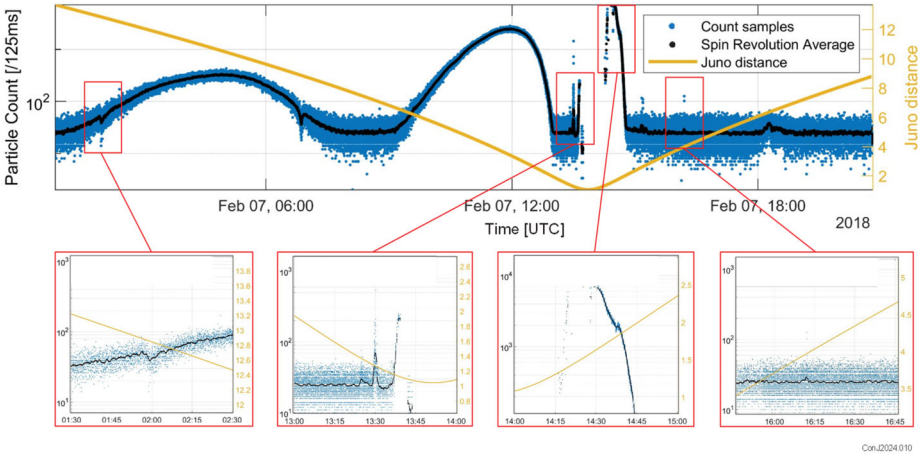

Fig. 12 Top: EPC time series along the PJ-11 trajectory with a full spacecraft rotation average marked in black. The broad bulges around 04:00 and 12:00 are due to the Jovian main magnetic dipole axis being offset from the rotation axis, causing Juno to pass in and out of radiation belt throughout the low latitude in-bound trajectory as the planet rotates. The orange curve shows Juno distance from Jupiter in Rj. Bottom: Four zooms of the time series showing disturbances or interactions. First (leftmost): Crossing of the magnetic field lines that crosses Ganymede orbit close to Ganymede. Second: Disturbances passing field lines close to the magnetic north pole. Third: Passing the southern radiation belt horn. Fourth: Sporadic interactions typically observed outbound

7 Conclusion

The ASC star tracker has been recording energetic particle count data from the Juno spacecraft since Jupiter orbit insertion. A calibration model for the count statistics, sensor sensitivity and shielding attenuation has been derived to describe the energetic particle omniflux from the CCD image particle count product. The ASC energetic particle count rate spans several orders of magnitude and provides a nearly continuous record at very high temporal resolution (4 Hz). It provides some visibility into the radiation environment at energies beyond the calibrated energy range of Juno's dedicated particle instruments (Mauk et al. 2017; McComas et al. 2017).

The potential of the omniflux product to be used for absolute mapping of the Jovian particle environment is demonstrated. Further, local signatures in the omniflux product may be employed as proxies for studying related phenomena. For example, Connerney et al. (2020) used the ASC particle counts to trace magnetic field lines over great distances (between the Juno spacecraft and Galilean satellites) in the Jovian magnetosphere, providing independent assessment of the accuracy of their magnetodisc model field.

The technique, as successfully demonstrated in Jovian orbit, is immediately scalable to other environments. It has been successfully operated on both the NASA Magnetospheric Multiscale Mission constellation star trackers (Shulman et al. 2018), and the ESA Swarm constellation star trackers (Toldbo et al. 2022).

Declarations

Competing Interests The authors declare no competing interests.

References

Allison J, et al (2016) Recent developments in geant4. Nucl Instrum Methods Phys Res, Sect A, Accel Spectrom Detect Assoc Equip 835:186–225. https://doi.org/10.1016/j.nima.2016.06.125

Becker HN, Alexander JW, Adriani A, Mura A, Cicchetti A, Noschese R, Jørgensen JL, Denver T, Sushkova J, Jørgensen AH, Benn M, Connerney JEP, Bolton SJ, The Selex Galileo Juno SRU Team, Allison J, Watts SJ, Adumitroaie V, Manor-Chapman EA, Daubar IJ, Lee C, Kang SS, McAlpine WJ, Di Iorio T, Pasqui C, Barbis A, Lawton P, Spalsbury L, Loftin S, Sun J (2017) The Juno radiation monitoring (RM) investigation. Space Sci Rev 213(1–4):507–545. https://doi.org/10.1007/s11214-017-0345-9

Berger MJ, Coursey JS, Zucker MA, Chang J (2017) Stopping-Power & Range Tables for Electrons, Protons, and Helium Ions. NIST Standard Reference Database 124. NISTIR 4999. https://doi.org/10.18434/T4NC7P

Bolton SJ (ed) (2018) The Juno mission Springer, Dordrecht

Connerney JEP, Benn M, Bjarno JB, Denver T, Espley J, Jorgensen JL, et al (2017) The Juno magnetic field investigation. Space Sci Rev 213(1–4):39–138. https://doi.org/10.1007/s11214-017-0334-z

Connerney JEP, Timmins S, Herceg M, Joergensen JL (2020) A Jovian magnetodisc model for the Juno era. J Geophys Res Space Phys 125:e2020JA028138. https://doi.org/10.1029/2020JA028138

de Soria-Santacruz M, Garrett HB, Evans RW, Jun I, Kim W, Paranicas C, Drozdov A (2016) An empirical model of the high-energy electron environment at Jupiter. J Geophys Res Space Phys 121(10):9732–9743. https://doi.org/10.1002/2016JA023059

Divine N, Garrett HB (1983) Charged particle distributions in Jupiter's magnetosphere. J Geophys Res 88(A9):6889–6903. https://doi.org/10.1029/JA088iA09p06889

Drouin D, Couture AR, Joly D, Tastet X, Aimez V, Gauvin R (2007) CASINO V2.42—a fast and easy-to-use modeling tool for scanning electron microscopy and microanalysis users. J Scanning Microsc 29(3):92–101. https://doi.org/10.1002/sca.20000

ECSS (2010) Calculation of radiation and its effects and margin policy handbook. ECSS handbooks, vol ECSS-E-HB-10-12A. European Cooperation for Space Standardization. https://ecss.nl/hbstms/ecss-e-hb-10-12a-calculation-of-radiation-and-its-effects-and-margin-policy-handbook/. Accessed 4 September, 2024

Garrett HB, et al (2003) Galileo interim radiation electron model. JPL Publication 03-006. Jet Propulsion Laboratory, California Institute of Technoly, Pasadena, CA

Herceg M, Jørgensen JL, Merayo JMG, Denver T, Jørgensen PS, Benn M, Kotsiaros S, Connerney JEP, Bolton SJ (2022) Energetic electron lensing caused by Ganymede's magnetic field. Planet Space Sci 224:105597. https://doi.org/10.1016/j.pss.2022.105597

Hubbell JH, Seltzer SM (2004) X-ray mass attenuation coefficients. NIST Standard Reference Database 126. NISTIR 5632. https://doi.org/10.18434/T4D01F

Ivanchenko V, et al on behalf of the Geant4 Collaboration (2019) Geant4 electromagnetic physics progress. In: 24th international conference on computing in high energy and nuclear physics (CHEP 2019). EPJ Web Conf 245:02009. https://doi.org/10.1051/epjconf/202024502009

Jun I, Garrett HB (2005) Comparison of high-energy trapped particle environments at the Earth and Jupiter. Radiat Prot Dosim 116(1–4):50–54. https://doi.org/10.1093/rpd/nci074

Mauk BH, Haggerty DK, Jaskulek SE, et al (2017) The Jupiter Energetic Particle Detector Instrument (JEDI) Investigation for the Juno Mission. Space Sci Rev 213(1–4):289–346. https://doi.org/10.1007/s11214-013-0025-3

McComas DJ, et al (2017) The Jovian auroral distributions experiment (JADE) on the Juno mission to Jupiter. Space Sci Rev 213:1–4. https://doi.org/10.1007/s11214-013-9990-9

Shulman S, Letoruneau S, Placanica S, Denver T, Jørgensen J (2018) Turning MMS star sensors into high energy particle detectors. In: Proceedings of 15th international conference on space operations, AIAA 2018-2714, American Institute of Aeronautics and Astronautics, 2018 SpaceOps conference, Marseille, France, 28/05/2018. https://doi.org/10.2514/6.2018-2714

Toldbo C, Sushkova J, Herceg M, Denver T, Benn M, Jørgensen PS, Merayo JMG, Jørgensen JL, Qamili E, Hoyos B, Haagmans R, Vogel P, Floberghagen R, Strømme A (2022) Mapping high energy particles using augmented star trackers on-board Swarm. Space Sci Rev 218(8):58. https://doi.org/10.1007/s11214-022-00925-z

Vavilov VS, Ukhin NA (1977) Experimental study of radiation defects in semiconductors and control of semiconductor properties by irradiation. In: Radiation effects in semiconductors and semiconductor devices. Springer, Boston, pp 30–102. https://doi.org/10.1007/978-1-4684-9069-5_2